# Insight into the degradation mechanisms of Atomic Layer Deposited $TiO_2$ as photoanode protective layer.

*Carles Ros*[a,*], *Nina M. Carretero*[a], *Jeremy David*[c], *Jordi Arbiol*[c,d], *Teresa Andreu*[a,*], *Joan R. Morante*[a,b]

[a] Catalonia Institute for Energy Research (IREC). Jardins de les Dones de Negre 1, 08930 Sant Adrià del Besòs, Barcelona, Spain

[b] Universitat de Barcelona (UB), Martí i Franquès, 1, 08028 Barcelona, Spain

[c] Catalan Institute of Nanoscience and Nanotechnology (ICN2), CSIC and BIST, Campus UAB, Bellaterra, 08193 Barcelona, Spain

[d] ICREA, Pg. Lluís Companys 23, 08010 Barcelona, Spain

KEYWORDS

$TiO_2$, water splitting, photoanode, protective layer, ALD, degradation.

**ABSTRACT**

Around 100 nm thick $TiO_2$ layers deposited by atomic layer deposition (ALD) have been investigated as anticorrosion protective films for silicon based photoanodes decorated with 5 nm NiFe catalyst in highly alkaline electrolyte. Completely amorphous layers presented high resistivity, meanwhile the ones synthetized at 300ºC, having a fully anatase crystalline $TiO_2$ structure, introduced insignificant resistance, showing direct correlation between crystallization degree and electrical conductivity. The conductivity through crystalline $TiO_2$ layers has been found not to be homogeneous, presenting preferential conduction paths attributed to grain boundaries and defects within the crystalline structure. A correlation between the c-AFM measurements and grain interstitials can be seen, supported by HRTEM cross sectional images presenting defective regions in crystalline $TiO_2$ grains. It was found that the conduction mechanism goes through the injection of electrons coming from water oxidation from the electrocatalyst into the $TiO_2$ conduction band. Then, electrons are transported to the $Si/SiO_x/TiO_2$ interface where electrons recombine with holes given by the $p^+n$-Si junction. No evidences of intra band gap states in $TiO_2$ responsible of conductivity have been detected. Stability measurements of fully crystalline samples over 480 h in anodic polarization show a continuous current decay. Electrochemical impedance spectroscopy allows to identify that the main cause of deactivation is associated to the loss of $TiO_2$ electrical conductivity, corresponding to a self-passivation mechanism. This is proposed to reflect the effect of $OH^-$ ions diffusing in the $TiO_2$ structure in anodic conditions by the electric field. This fact proves that a modification takes place in the defective zone of the layer, blocking the ability to transfer electrical charge through the layer. According to this mechanism, a regeneration of the degradation process is demonstrated possible based on ultraviolet illumination, which contributes to change the occupancy of $TiO_2$ electronic states and to recover the defective

zones conductivity. These findings confirm the connection between the structural properties of the ALD-deposited polycrystalline layer and the degradation mechanisms, and thus highlight main concerns towards fabricating long-lasting metal oxide protective layers for frontal illuminated photoelectrodes.

## 1. INTRODUCTION

Our society faces a significant challenge regarding energy production and climate change, where renewable energy sources are called to be crucial. However, the high variability on renewables such as wind and solar power is one of the main drawbacks nowadays. Storing solar energy into chemical bonds is an interesting candidate to face this variability, the so called "solar fuels".[1–4] Among them, hydrogen produced from water electrolysis is a promising candidate as energy vector, substituting natural gas as heat source[5] or fossil fuels used for transportation.[6] Photoelectrochemical (PEC) water splitting was discovered by Fujishima and Honda in the late 70's, [7] but solar to hydrogen (STH) efficiencies have been far from industrial requirements for decades, although remarkable efforts have been put in understanding and enhancing photoactive metal oxide semiconductors and catalysts to perform the water splitting reaction. [8–18]

With the significant increase in productivity and cost reduction of the photovoltaic industry, which has led to its large scale implementation, many authors have put their attention into implementing these semiconductor materials and fabrication methods in PEC water splitting. [19–21] Many materials such as monocrystalline[22–24] and amorphous silicon, [25] chalcogenide-based compounds,[26,27] III-V semiconductors[28–32] and even perovskites[33] have been proposed. However, all of these semiconductors face a common problem: the chemical stability of such materials when exposed to the highly acidic or alkaline electrolytes necessary for kinetically-efficient oxygen and hydrogen evolution reactions (OER and HER).[20] To overcome this, the use of protective layers was suggested, avoiding the contact between the electrolyte and the sensible photoabsorber materials, but their fabrication routes should assure that the photoabsorber suffers no harm or alteration. In addition, protective layers for frontal illuminated photoelectrodes need to be conductive, transparent, chemically stable. These requirements reduce the candidate

materials and methods. Among them, $TiO_2$ is found to be one of the best performing candidates,[21,34–38] and among deposition techniques, atomic layer deposition (ALD) allows high layer thickness control, conformal layers almost pinhole free, and low crystallization temperatures thanks to intermediate-species mobility, avoiding alterations of inner layers of the photoelectrode.[39–42] For instance, recent studies have reported interesting characteristics of ALD-$TiO_2$ such as increased adhesion on Si photoanodes[43] or enhanced plasmonic resonance in photovoltaic devices[44].

Photocathodes protected with polycrystalline $TiO_2$ have been widely reported as the conduction band alignment between the silicon and the $TiO_2$ metal oxide facilitates the electron transfer from the photocathode to the electrolyte through the $TiO_2$ layer that is n-type. [22,26,45–49]

Regarding $TiO_2$ protecting silicon based photoanodes, there is a totally different casuistic. In this case, the photo-generated minority carriers, holes, must be transferred to the electrolyte through a protective n-type $TiO_2$ layer. Different works have studied $TiO_2$ as protective layer for photoanodes, mainly using silicon as the photoabsorbing material, either forming an heterojunction between the $TiO_2$ and the n-Si[50–55] or with a buried $p^+$-n junction in silicon. [28,56,57] Under these boundaries, as a n-type metal oxide layer was expected to be highly resistive when thicker than the tunnelling distance, first works with $TiO_2$ grown via ALD as protective layer were using thicknesses ranging of only few nanometers. [50,51,55,57,58] However, these assumptions were put in evidence by the studies carried out by Hu *et al*. [28] These authors used layers with thicknesses over 100 nm which were found to have conductivity enough to validate the use of $TiO_2$ for photoanodes as feasible. They propose state-mediated hole transport through intra-band gap levels as the conduction path caused by the disorder of amorphous $TiO_2$ ("electronically

leaky layer"), in alignment with the silicon valence band, following the same mechanism postulated decades ago by Campet et al. [59]

Other authors that claim not identifying this mid bandgap levels in their samples have proposed a mechanism based on a MIM-like (Metal-Insulator-Metal) structure defined by a $TiO_2$ layer between the photoabsorber and the electrocatalyst. Thus, Mei et al. [56] proposed that electrons were conducted through the conduction band for a p+-Si/Ti/$TiO_2$/Pt structure. So, under this model, electrons from the oxygen evolution reactions through the electrocatalyst are easily injected to the conduction band of the titanium oxide layer and transferred to the internal Si/$TiO_2$ interface at the photoanode where they recombine with the photogenerated holes. However, these works generally do not consider the polycrystalline nature of the $TiO_2$ layer and neither their degradation mechanisms, which they are often overlooked.

In this context, this work aims at revealing the role of the amorphous / polycrystalline nature of the atomically deposited $TiO_2$ layer, considering its defective zones, to determine the electrical conductivity pathways and their evolution over time as a consequence of the degradation mechanisms that take place, which determines the endurance to the use of the protective layers based on $TiO_2$ in silicon photoanodes for water splitting.

## 2. EXPERIMENTAL SECTION

$TiO_2$ coatings have been grown by ALD on $p^+$-n silicon buried junctions and simultaneously on $p^+$ degenerately doped silicon, to simulate direct injection of carriers in dark conditions.

$p^+$-Si samples were created by cutting a degenerately doped silicon wafer (0.001 Ω·cm) in 1x1 $cm^2$ pieces, and 50 nm of Al were thermally evaporated as back contact.

For the $p^+n$-Si samples, a 1 $cm^2$ active area was lithographically defined by $SiO_2$ passivation on a silicon n-type wafer (0.1-0.5 Ω.cm resistivity). Boron was implanted in the defined front surface and activated by rapid thermal annealing, creating a 200 nm $n^+$ region on top of the n-type substrate. As back contact, 1 µm of Al/0.5%Cu was sputtered on top of 30 nm of Ti to form a proper ohmic contact.

$p^+$-Si and $p^+n$-Si samples were sonicated for 5 min in a 1:1:1 isopropanol, acetone and DI water cleaning solution, followed by abundant rinsing and further 5 min sonication in DI water. Before ALD deposition, front surface was cleaned with 0.1M HF for 5 min, rinsed in DI water and immediately introduced in the ALD chamber.

A R200 Picosun Atomic Layer Deposition system was used to grow $TiO_2$ layers. $TiCl_4$ was selected as precursor because of its wide deposition window and lower cost compared with other metalorganic compounds. Thus, $TiCl_4$ and $H_2O$ precursors at 19 ºC were used in successive pulses at 8 mbar in $N_2$ flow atmosphere, with 0.1 s pulses and 10 s purges. Under these conditions, layers were grown at deposition temperatures of 100, 150 and 300 ºC for 3300 cycles, corresponding to roughly 100 nm layers. Layer thickness was measured by evaluating the reflected spectra with a Sensofar interferometer device with ± 0.2 nm error. Finally, nickel-iron (NiFe) was deposited by thermal evaporation using an Oerlikon Univex 250 equipment, with a thickness of 5 nm measured by a quartz microbalance. Samples were then soldered to a Cu wire using Ag paint and epoxy protected leaving the front area exposed (Figure S1).

Surface morphology was observed with a Zeiss Series Auriga Field Emission Scanning Electron Microscope (FESEM). Structural characterization was carried out by X-ray diffraction (XRD) in a D8 Advance Bruker equipment with a Cu $K_\alpha$ radiation source working at 40 kV and 40 mA with a 3 º offset angle. Raman spectroscopy was performed using a Horiba LabRam HR 800 with 532 nm laser light with a 100x objective and an output power of 5 mW, 10 s acquisition time and 10 accumulations. High resolution transmission electron microscopy (HRTEM), high angle annular dark field (HAADF) scanning TEM (STEM) and electron energy loss spectroscopy (EELS) spectrum imaging (S.I.) were performed using a TECNAI F20 operated at 200 kV with a point to point resolution of 0.19 nm, with a coupled GATAN QUANTUM EELS detector. HRTEM samples were prepared using a focused ion beam (FIB) to select the desired region to image, previous protecting the surface with deposited Pt. AFM and conductivity AFM (c-AFM) measures were taken with a Park Systems XE-100 with platinum conductive cantilevers biasing the sample at +1 V. Due to the $p^+n$-Si built-in voltage, only the samples on $p^+$-Si substrates were measured by c-AFM. The photoelectrochemical measurements (cyclic voltammetries, chronoamperometries and electrochemical impedance spectroscopy) were obtained with a Biologic VMP-300 potentiostat using Ag/AgCl/KCl (3M) ($E^0$ = 0.203 $V_{RHE}$) as reference electrode and platinum mesh as counter electrode. A quartz cell with flat faces was used with 100 ml of 1M KOH electrolyte and a 300 W xenon lamp with an AM 1.5G filter adjusted to 100 $mW/cm^2$, calibrated using a silicon diode (Gentec-EO, XLPF12-3S-H2-DO). 20 $mW \cdot cm^{-2}$ 365 nm UV light is obtained from a 200 W Hg-Xe Hamamatsu LC8 light source lamp. I-V curves were obtained in two-electrode configuration depositing 50 nm of Au as top contact.

## 3. RESULTS AND DISCUSSION

### *3.1. Morphological and structural characterization*

In this work, we have fabricated silicon photoanodes protected with $TiO_2$ layers prepared by Atomic Layer Deposition (ALD) in a temperature range from 100 to 300 ºC from $TiCl_4$ precursor, which permits a wide temperature deposition window.[60]

Figure 1 shows SEM surface images of the ALD $TiO_2$ coatings synthetized at the different temperatures. For the film obtained at 100ºC (Figure 1a), a homogeneous coating is observed with no presence of grains, whereas using deposition temperatures of 150 ºC some regions with different contrast appear, corresponding to grains embedded in an amorphous matrix (Figure 1b). Further increasing deposition temperature up to 300 ºC (Figure 1c), yields to a highly crystalline surface with smaller grain sizes. These grains are related to the $TiO_2$ anatase phase, as can be seen in the XRD diffraction pattern for the sample synthetized at 300ºC (Figure 1d). The $TiO_2$ anatase phase is more favourable to $OH^-$ adsorption and thus causing higher ALD growth rate.[22,61] No anatase XRD peaks or other crystalline phases are detected at 100 or 150 ºC, as previously observed in literature.[53,62]

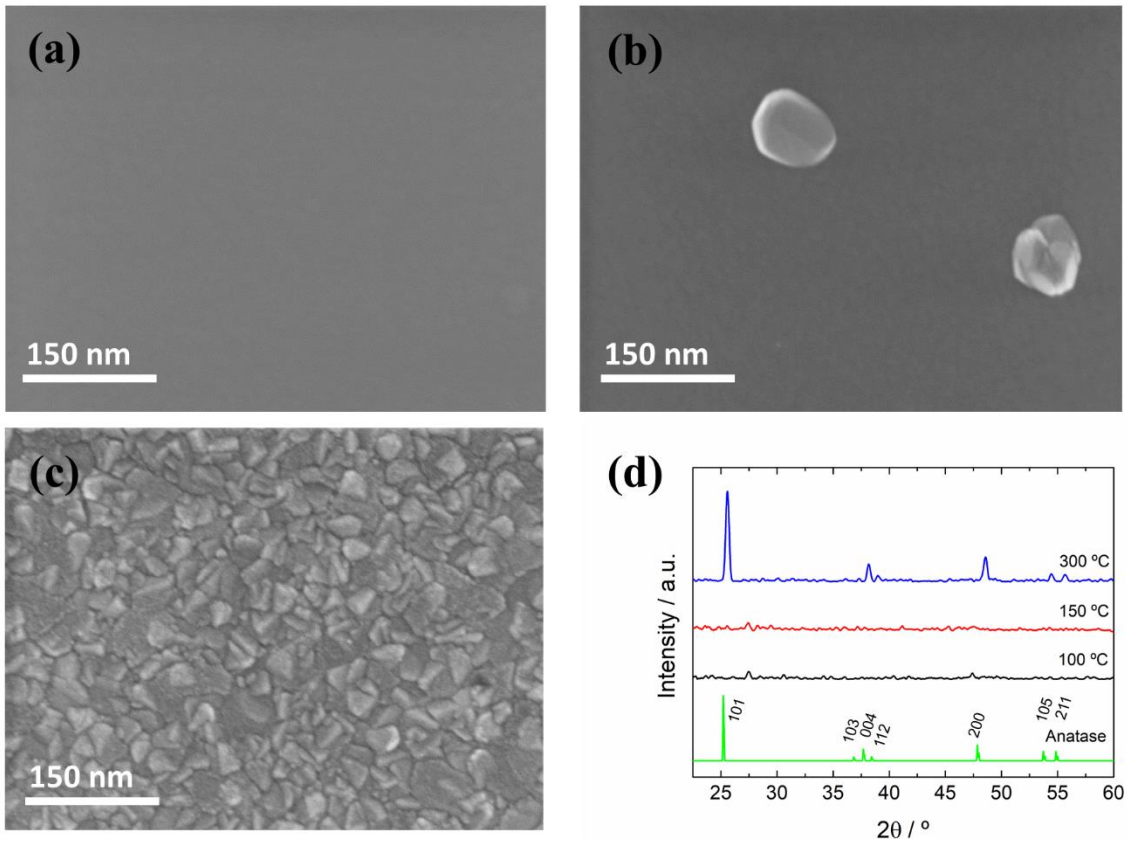


**Figure 1.** Top view SEM images of $n^+p$-Si photoanodes protected with 100 nm $TiO_2$ grown at 100 ºC (a), 150 ºC (b) and 300 ºC (c). (d) XRD spectra of $TiO_2$ layers grown at 100 ºC (black), 150 ºC (red) and 300 ºC (blue) compared to the reference anatase pattern RRUFF R060277.9 (green).

As it can be seen in the SEM image for the sample synthetized at 150ºC (Figure 1b) the density of embedded crystals is rather low, and therefore XRD measurement does not allow the identification of the crystalline structure, being below the resolution. We used Raman spectroscopy equipped with an optical microscope, in order to carry out a more localised analysis. Optical view of the Si chip with an ALD-$TiO_2$ layer grown at 150 ºC is shown in Figure 2a, were it is seen the presence of dark spots embedded in a homogenous grey film, which may be attributed to the submicron size crystals identified by SEM. [63] Figure 2b presents the Raman

spectra of two different spots, with a clear appearance of an intense peak in the darker spot, corresponding to the Eg mode of anatase located at 141.4 $cm^{-1}$. The peak is red-shifted with respect to the expected 144 $cm^{-1}$ value,[64] being a sign of tensile stress, probably caused by partial amorphousness of the interface and reduced crystalline size.[65] A Raman mapping scan of the Eg main peak is shown in the inset of Figure 2a, which allows us to correlate the dark spots seen in the optical image with anatase crystallographic order presence.

Complete analysis by micro Raman spectroscopy of $TiO_2$ layers grown at 100, 150 and 300 ºC is shown in Figure 2c. None of the spots analyzed of the sample synthetized at 100ºC present the anatase peak, whereas is present at any spot at 300 ºC samples, confirming the existence of a fully polycrystalline layer, in accordance with the XRD results and SEM. A deeper analysis of the Raman spectra shows a more intense peak for 300 ºC layers compared with 150ºC crystalline zones, and a blue shift of the Eg mode (of 10.3 $cm^{-1}$), that can be attributed to either surface pressure or phonon confinement effect that usually exist in nanometer-sized materials.[66] As seen in SEM images (Fig. 1c), nucleation is enhanced with increased deposition temperature and smaller grains are obtained by competitive growth.

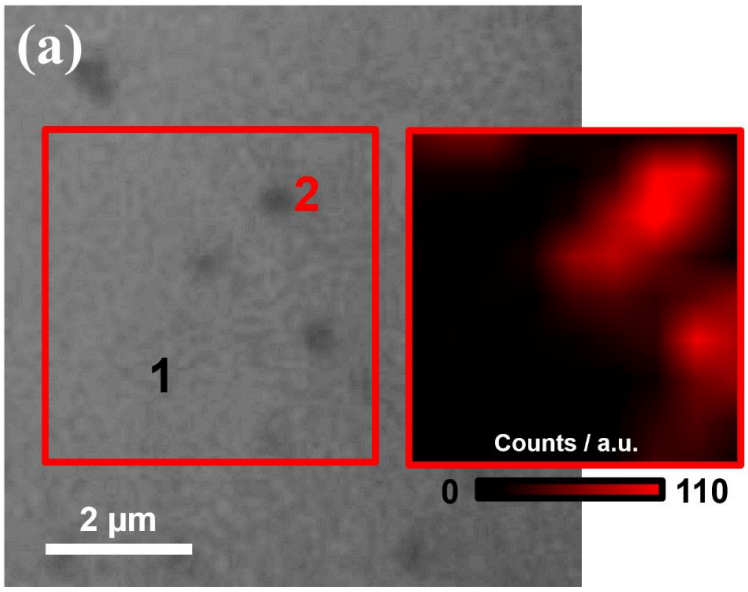
(a)
2
1
Counts / a.u.
0
110
2 μm

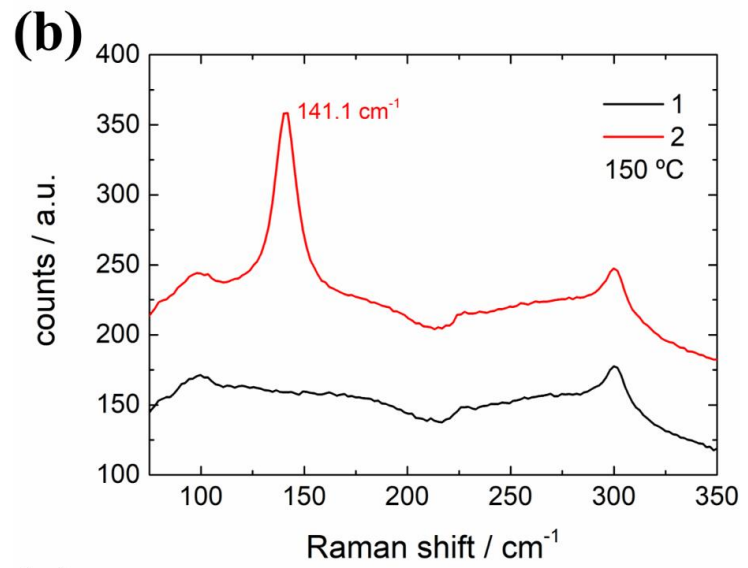
(b)
141.1 cm-1
1
2
150 ºC
counts / a.u.
Raman shift / cm-1

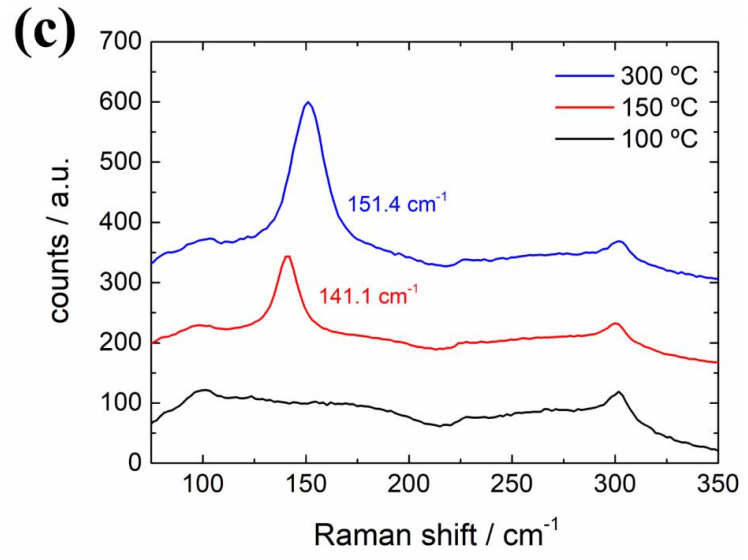
(c)
300 ºC
150 ºC
100 ºC
151.4 cm-1
141.1 cm-1
counts / a.u.
Raman shift / cm-1

**Figure 2.** (a) Optical image of a protected silicon with $TiO_2$ grown by ALD at 150 ºC. Right inset, counts map of the Eg Raman shift of the indicated region. (b) Raman shift spectra of two different positions of image a) corresponding to an amorphous region (1, black) or a crystalline grain (2, red). c) Raman shift spectra of ALD-$TiO_2$ layers grown at 100 ºC (black), 150 ºC (red) and 300 ºC (blue). The presented Raman shift spectra for the sample synthesized at 150 ºC corresponds to a position where a $TiO_2$ grain can be seen. Peak maximum position is indicated for 150 and 300 ºC.

### *3.2. Electrochemical characterization*

In Figure 3a, cyclic voltammetries of three illuminated $p^+n$-Si homojunctions are shown. The photoanodes, previously cleaned with HF (to eliminate the $SiO_x$) and immediately ALD-protected with $TiO_2$ grown at 100, 150 and 300 ºC were then coated with a 5 nm film of thermally evaporated NiFe, to act as OER catalyst. For samples grown at 100 ºC, no photocurrent can be observed. However, for samples deposited at 150ºC and 300ºC the same onset potential is obtained (around 0.96 V vs RHE) and whereas significant photocurrent is obtained for the former, highly increased currents are observed for the later. This fact, together with the saturation regime reached at more anodic potentials for the 150 ºC sample, indicate a more resistive layer. The saturation current value, 22.5 $mA/cm^2$, is given by the photovoltaic quality of the prepared silicon-based homojunctions that were not optimized, and the lack of adjusted antireflective strategies.[67]

In dark conditions, the same tendency observed for photoanodes is obtained in $TiO_2$-protected $p^+$-Si anodes: increasing deposition temperature from 150 to 300 ºC enhances OER current

(Figure 3b). The nickel-iron catalyst is necessary for efficient charge injection into the electrolyte [28,68–71], and if it is not present, no oxidative current is obtained in the studied range of potentials (dotted line in Figure 3b). In fact, Ni(Fe)OOH is the real catalytic phase obtained after cycling in alkaline electrolytes such as standard KOH solutions, one of the earth-abundant OER catalyst with lower overpotentials [38,72–81]. The voltage difference between oxidative and reductive redox peaks of Ni hydroxide/oxyhydroxide is decreased when increasing $TiO_2$ deposition temperature (0.592 and 0.216 V for 150 and 300 ºC). This fact is in accordance with the slopes of the OER current both in photoelectrodes (Figure 3a) and electrodes (Figure 3b), and it is related to higher series resistance in the system. Likewise, $Ni^{2+}/Ni^{3+}$ redox peaks present smaller area for the 150 ºC sample than for the one synthesized at 300 ºC, which indicates less active catalyst in the former sample, as the deposited NiFe quantity is the same in both samples. This fact may point out that charge transfer is boosted in the 300ºC sample in comparison with the 150ºC one.

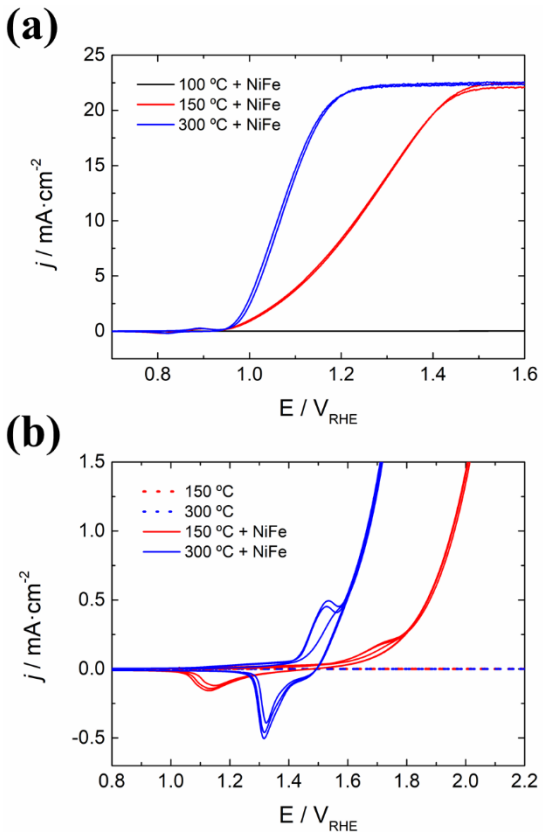


**Figure 3.** (a) Cyclic voltammetries (1 sun AM 1.5G) of $p^+n$-Si photoanodes protected with 100 nm $TiO_2$ layers grown at 100 ºC, 150ºC and 300 ºC, with 5 nm of nickel-iron thermally evaporated as OER catalyst. (b) Cyclic voltammetries in dark of $p^+$-Si substrates protected either with 150ºC or 300 ºC $TiO_2$ layers and decorated or not with 5 nm of thermally evaporated nickel-iron. 1 M KOH was used as electrolyte.

### *3.3. Conduction pathways in $TiO_2$-ALD protected photoanodes*

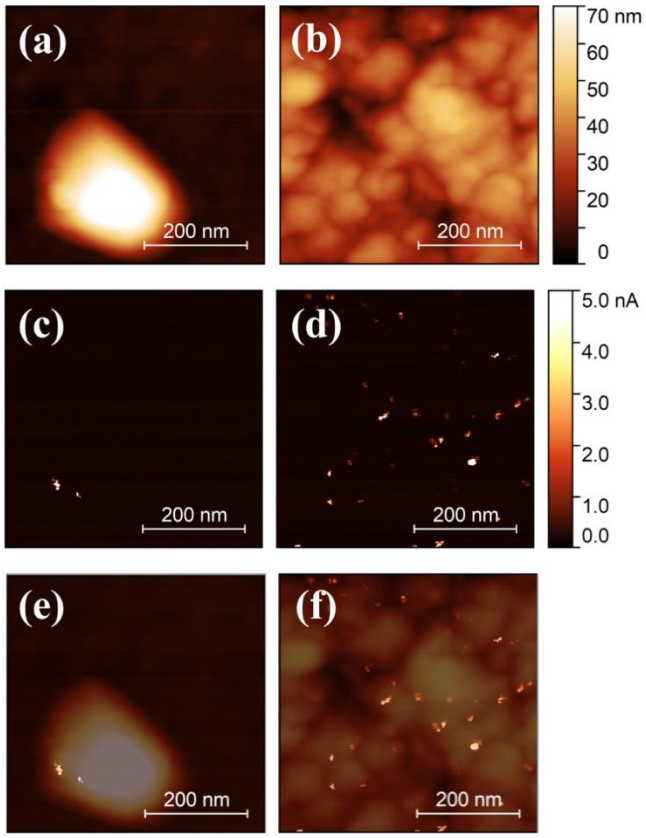


**Figure 4.** AFM height map of $TiO_2$ + NiFe layers grown at 150ºC (a) and 300 ºC (b), and its respective current intensity maps, (c) and (d) obtained at +1 V. (e) and (f) shows the overlays of the topography and current maps for each sample.

In Figure 4, we present the topography and conductivity atomic force microscopy maps (c-AFM) of ALD-$TiO_2$ samples grown on degenerately doped $p^+$-Si substrates at 150 ºC and 300 ºC with 5 nm NiFe thermally evaporated on top. Measurements of $TiO_2$/NiFe layers were performed at +1 V, simulating the electron flow from the tip to the substrate across the layer, like in OER anodic conditions. Without NiFe catalyst, no current could be measured in the used range of potentials. As it can be seen in Figure 4 e-f, there is a correlation between topography maps and regions where current signal is detected: crystalline boundary regions, more abundant in the 300 ºC sample than in the 150 ºC, and no current in the amorphous regions. Additional images pointing

in the same direction are presented in supporting information Figure S2. Localized conduction of $TiO_2$-ALD layers observed by c-AFM has been also reported by other works. To explain the preferential conduction paths, Yu et. al.[82] suggested the presence of crystallographically metastable regions, and Murakami et. al.[83] assumed an inhomogeneous distribution of oxygen vacancies (Vox) known to be mobile under applied potentials and capable to agglomerate, defining preferential electron trap-assisted tunneling conductivity paths or conductive filaments, or Magneli phases in the grain boundaries such as it has been identified in the development of $TiO_2$ memristors.[84–87]

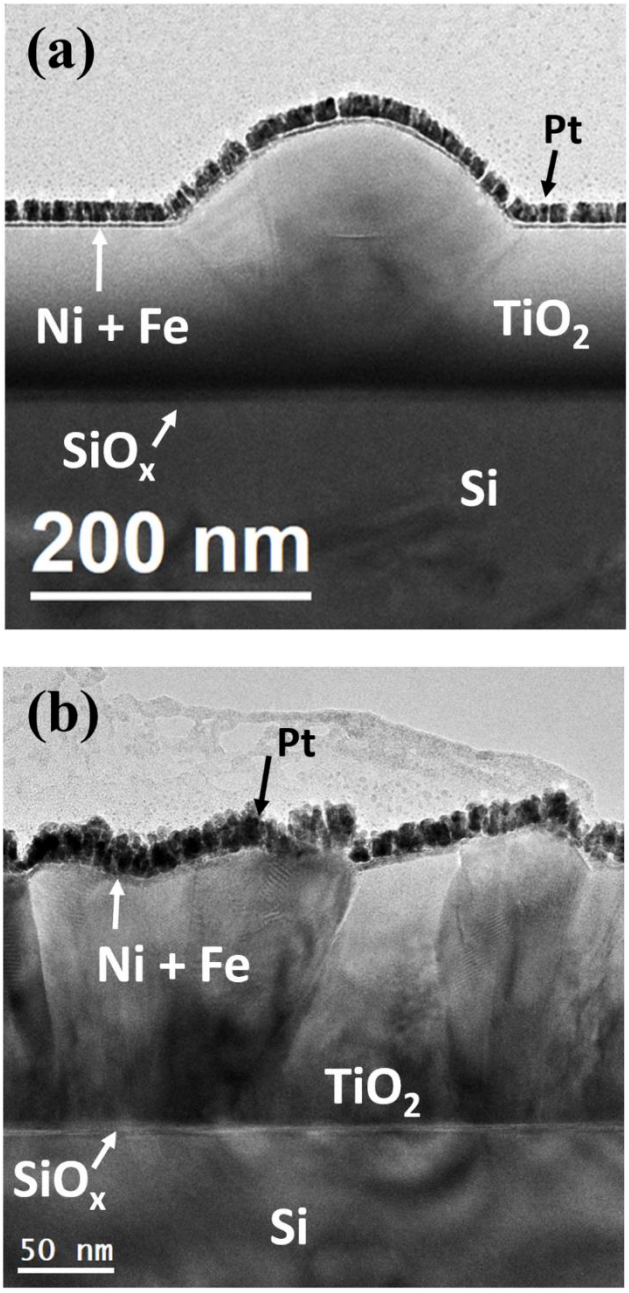


**Figure 5.** HRTEM cross sectional images of $TiO_2$ layers grown by ALD at 150 ºC (a) and 300 ºC (b). A Pt layer was deposited on top to protect the sample during the FIB sample preparation process.

Figure 5 shows the HRTEM images of the cross section obtained by FIB for the samples synthetized at 150 and 300ºC, where multiple crystal orientations, grain boundaries and twin-like defects can be seen, embedded in an amorphous matrix for the 150 ºC sample . Thus, unevenly distributed defects and oxygen vacancies should be expected, affecting the electrical states distribution. More HRTEM analysis is further depicted in Figure S3.

Columnar grains are present in both samples synthesized at 150 and 300 ºC, but nucleation is significantly different. The HRTEM image of the sample grown at 150 ºC shows that $TiO_2$ is crystalline only in a few-nanometer dome-like region close to the substrate, while the rest of the $TiO_2$ layer remains amorphous. However, the one prepared at 300 ºC shows that the whole $TiO_2$ layer is crystalline. This can be attributed to the higher deposition temperature used, which enhances nucleation and lateral crystal propagation, together with crystal competition.[41]

The $TiO_2$/NiFe interface can be analysed by HRTEM EELS. In those as-prepared samples, the ~5nm apparently homogeneous NiFe catalyst layer can be seen (Figure S4a). After cycling in 1 M KOH (Figure S4b), a thicker layer can be observed, and the oxygen presence throughout the whole NiFe layer is increased, indicating oxidation of the metallic layer and $OH^-$ incorporation, as reported in other works, where a restructuration of the NiFe towards a three dimensional nanoflakes porous layer takes place.[88] Moreover, there is no presence of Ni or Fe incorporation in the $TiO_2$ crystalline structure, or O or Ti concentration gradient can be detected above the EELS system resolution threshold, neither in the amorphous or crystalline structures nor the grain boundaries (Figures S5, S6).

To study the surface chemical composition of the layer, XPS analysis was performed, which is discussed in the supplementary information and Figure S7. To sum up, for as prepared samples, a

2.8:1 Ni:Fe ratio is observed, natively oxidized before anodic cycling and with higher oxygen content afterwards, caused by $OH^-$ intercalation and oxidation of the coatings. Ni 2p spectra presents Ni(0) metallic peaks before but not after immersion in the electrolyte. For the cycled sample, multiple Ni(II) and Ni(III) peaks can be fitted (Figure 7a), probably by the presence of multiple chemical states such as NiO, $Ni(OH)_2$ and NiOOH, not easy to differentiate by XPS[89], and also correlated to Fe(III) forming Ni(Fe)OOH, as reported in other works[38,69,88,90–92].

XPS analysis also allows to obtain valence band (VB) positions of the superficial electrons, through the density and occupancy of electronic states of the surface (Figure S8). On one hand, as prepared $TiO_2$ layers at 150 and 300 ºC present valence band potentials of ~2.75 eV under Fermi level, pointing at a higher n-type behaviour for the sample grown at 300 ºC (larger Fermi level to valence band energies). On the other hand, no signal from intra-bandgap states is detected with a fine analysis of the 0-3 eV region in accordance with another works [28], although the small signal-to-noise ratio could be hindering the detection (Figure S9). Also, the oxidation of the metallic NiFe layer after immersion in the electrolyte at anodic potentials is revealed by the XPS spectra, still presenting slight free electrons behaviour. The most significant result is the excellent band alignment between $TiO_2$ conduction band and the Ni(Fe)OOH catalyst, that justify the injection of electrons from the oxygen evolution catalyst to the $TiO_2$ conduction band. The results obtained can be summarized in the mechanism proposed in Scheme 1, basing the conductivity in preferential charge transport pathways. The increased conductivity pathways density present for 300 ºC deposited samples with respect to 150 ºC ones (Figure 4 e-f) must be especially highlighted, in agreement with reported data in Figure 3. In addition, several features can be underlined:

1) The Si-$TiO_2$ interface has been found not to introduce significant electrical barrier to charge transport. A recombining contact for holes from the $p^+$-Si valence band and electrons from the $TiO_2$ preferential paths conduction band is expected, facilitated by tunnelling through the ALD-caused $SiO_x$ similar to the schemes proposed by other authors.[93]

2) The transversal section to charge transport has been proven to be not homogeneous. Lower resistivity regions detected by c-AFM are attributed to more defective crystalline $TiO_2$ regions than bulk crystal grains, forming preferential conductivity paths through the grain boundaries and defects within the crystalline structrure.[84]

3) There is a favourable electron transfer from the Ni(Fe)OOH to the $TiO_2$ conduction band. This is facilitated by the permeable to electrolyte and energetically adaptive characteristics of the catalyst due to ionic diffusion, avoiding the energetic barrier formed between $TiO_2$ and the electrolyte and facilitating OER reaction. [69,46]

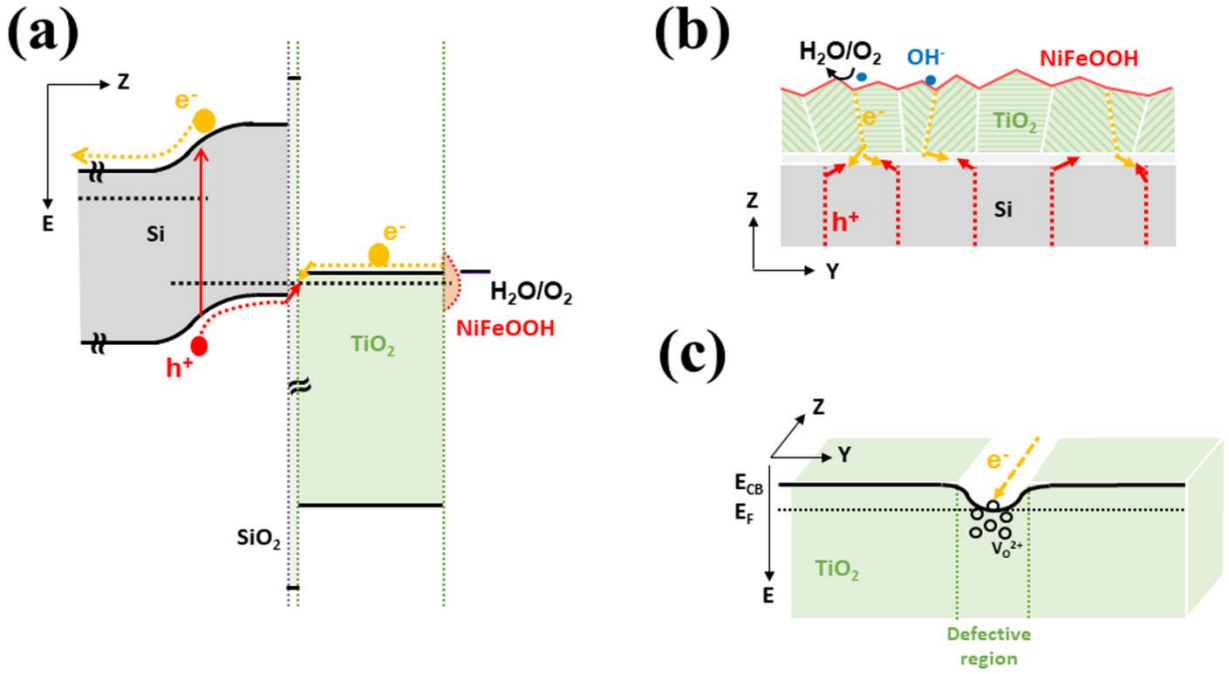

**Scheme 1.** (a) Band diagram of a $p^+$n-Si photoanode, $TiO_2$ protected with cycled Ni(Fe)OOH catalyst. (b) Cross section diagram with electron and holes flow paths depicted. c) Energy and cross section diagram corresponding to a preferential path or defective region, showing how extra states in interfacial defects generate a preferential path.

### *3.4. Endurance test: degradation mechanisms and stability*

Crystalline $TiO_2$-protected $p^+$-Si anodes and $p^+$n-Si photoanodes were tested for stability in a 1 M KOH electrolyte at anodic potentials. The obtained current density values show significant decay for both electrodes (Figures 6 and 7). To further analyse these samples, Electrochemical Impedance Spectroscopy (EIS) was applied before and during stability test.

For the $p^+$-Si anode in dark conditions, the current measured for more than 480 h at 1.8 V vs RHE, shows an exponential decay (Figure 6a), which indicates a degradation of the electrode. The EIS measurement shows two clear semicircles increasing over time (Figure 6b) revealing degradation correlated with two processes in series defined by different RC time constants, which allows us to propose an equivalent electrical circuit shown in Figure 6b. As seen in Figure S10, the first semicircle ($R_2/C_2$) is independent from the applied potential and the second one varies significantly between open circuit potential (OCP) and OER working conditions, proving a non-ohmic dependence of this second one. Our electrode has been modelled to an ohmic resistance, $R_1$ (corresponding to all resistive system contributions given by cables, back contact and substrate and electrolyte conductivity), a $R_2/C_2$ parallel circuit in series (corresponding to the deplection region within the $TiO_2$ protective layer) and a Randles circuit ($R_3/CPE_3$, corresponding to the electrocatalytic OER charge transfer on Ni(Fe)OOH).

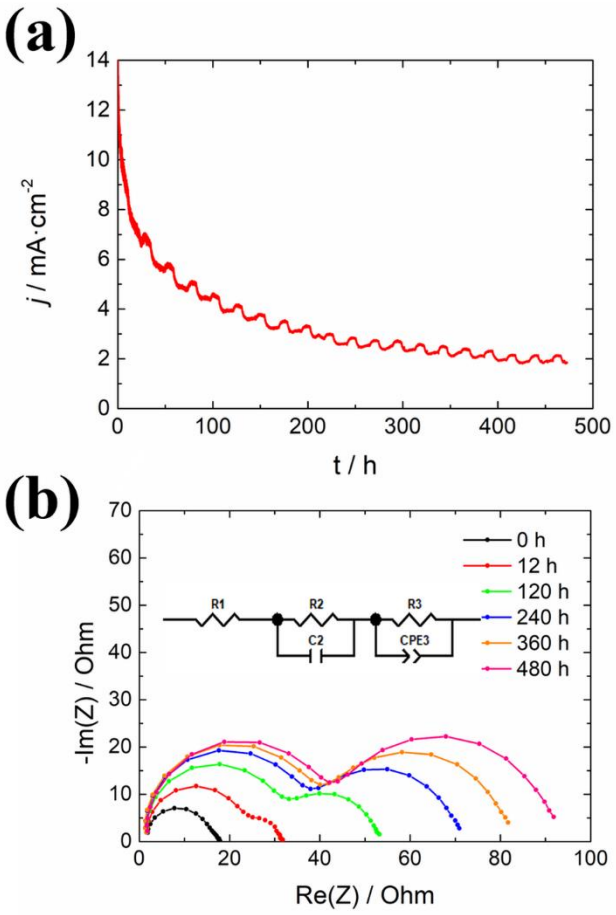


**Figure 6.** (a) Chronoamperometry of a $p^+$-Si anode protected with ALD-deposited $TiO_2$ at 300 ºC and NiFe decorated in 1 M KOH at a fixed potential of 1.8 V vs RHE. (fluctuations are due to daily temperature changes). (b) Nyquist plot of the electrochemical impedance spectroscopy (EIS) data from the same sample obtained every 12 h under potentiostatic 1.8 V vs RHE potential from 1 Hz to 50 kHz and an amplitude of 25mV. The inset shows the equivalent electric circuit used to fit the EIS data.

Fitting the proposed EIS circuit to our experiments (Table 1), a clear relation is observed between the current loss during stability tests and the semicircles increase. The current diminution rate is initially high, and it is reduced as current values decrease, pointing towards a relation between current passing and conductivity degradation. The resistance $R_2$ corresponding to the current flow

through the $TiO_2$ layer increases logarithmically over time at 1.8 V vs RHE, meanwhile $R_3$, the resistance attributed to charge transfer in the OER reaction, increases lineally (Figure S11).

**Table 1.** Values obtained after fitting the data presented in Figure 6b according to the circuit proposed.

| Time (h) | $R_1$ (Ω) | $R_2$ (Ω) | $C_2$ ($F \cdot cm^{-2}$) | $R_3$ (Ω) | $CPE_3$ ($F \cdot cm^{-2} \cdot s^{\alpha 3-1}$) | $\alpha_3$ |
|---|---|---|---|---|---|---|
| **0** | 1.40 | 13.56 | $2.11 \cdot 10^{-6}$ | 2.83 | $6.54 \cdot 10^{-4}$ | 0.787 |
| **12** | 1.33 | 22.58 | $1.80 \cdot 10^{-6}$ | 7.30 | $1.22 \cdot 10^{-4}$ | 0.992 |
| **120** | 1.22 | 31.32 | $1.83 \cdot 10^{-6}$ | 19.84 | $1.22 \cdot 10^{-4}$ | 0.955 |
| **240** | 1.03 | 37.04 | $1.84 \cdot 10^{-6}$ | 31.53 | $1.14 \cdot 10^{-4}$ | 0.955 |
| **360** | 0.92 | 39.30 | $1.79 \cdot 10^{-6}$ | 40.40 | $1.18 \cdot 10^{-4}$ | 0.940 |
| **480** | 1.29 | 40.37 | $1.67 \cdot 10^{-6}$ | 50.45 | $1.41 \cdot 10^{-4}$ | 0.901 |

Owing to the fact that the interfacial $SiO_x$ layer does not increase in thickness after stability test (Figure S12), the increase of $R_2$ over time can be related with the intrinsic self-passivating process of metal oxide surfaces, following a logarithmic rate law.[94] This is highlighting an interaction of $OH^-$ ions from the electrolyte and the polycrystalline $TiO_2$ driven by the electric field due to anodic polarization. Some authors have previously reported chemical interaction of $OH^-$ migration and defective regions, nulling preferential charge transport paths. [95]

The significant decrease of crystalline $TiO_2$ conductivity has not previously been stated, but a deep review of the bibliography does not deny its plausibility. Other works have shown the possibility of $OH^-$ to penetrate through a permeable Ni catalyst layer and diffuse through the $TiO_2$[82] or ALD-$TiO_2$ dissolution on few hours scale[95]. Oxygen mobility under polarization in $TiO_2$ has been known for years, forming preferential paths in the form of conductive filaments. [96,97] The presence of such oxidant molecules, $OH^-$, inside the $TiO_2$ structure can easily interact

with the states responsible of the n-type semiconductor properties and conductivity.[98] This fact has been depicted in Scheme S1a and b.

On the other hand, according to the Tafel equation describing the charge transfer at the electrode/electrolyte interface (eq. 1)[99], overpotential ($\eta$) depends logarithmically on the current density. Assuming both elements are in series ($i_2$ equals $i_3$, $i$), and the resistance of the $TiO_2$ layer ($R_2$) increases while applied potential is kept constant, the current reaching the OER reaction (measured in EIS as $R_3$) will decrease logarithmically, giving an inverse logarithmic dependence of $R_3$ with $R_2$ (eq. 2), represented in Figure S13. A 5 times increase in the total resistance ($R_2$ + $R_3$) is in accordance with the equivalent current reduction observed after the 480 h stability test under anodic polarization.

$$\log\left(\frac{1}{R_{ct}}\right) = \frac{di}{d\eta} = a * \eta + b; \quad (1)$$

where $R_{ct} = R_3$ and $\eta = V - i * R_2$ , giving:

$$\log\left(\frac{1}{R_3}\right) \propto (-R_2) \quad (2)$$

Following these equations, if $R_2 \propto \log(t)$ as it has been demonstrated in Figure S11, and substituting in eq. 2, we obtain $R_3 \propto t$ .

In his turn, capacitance of the $TiO_2$ semicircle is not significantly modified as expected, as it corresponds to the thickness and dielectric constant of the $TiO_2$ and these are maintained.

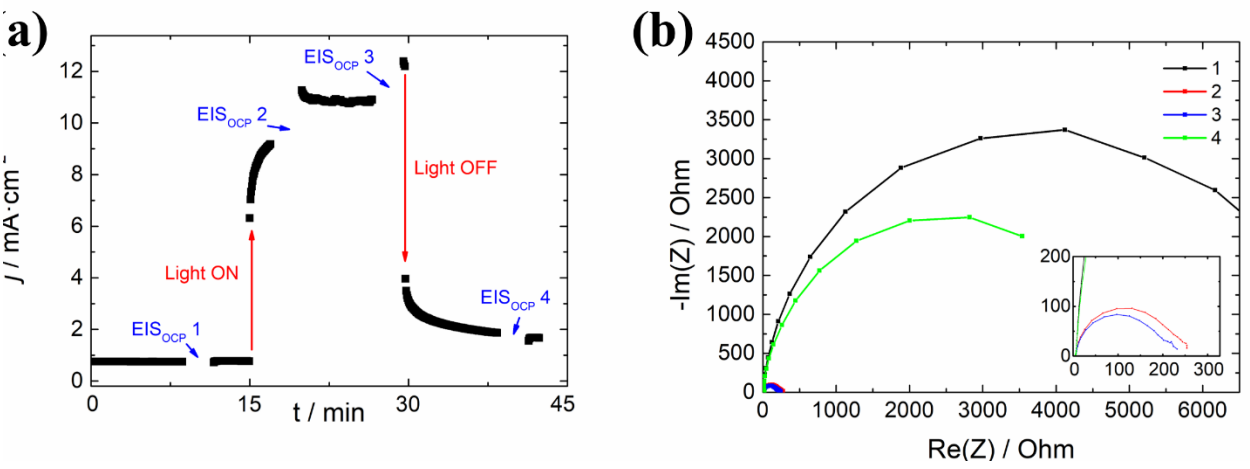


**Figure 7**. a) Chronoamperometry measurement at 1.3 V vs RHE of a $p^+$n-Si photoanode protected with $TiO_2$ ALD-deposited at 300 ºC and NiFe under solar irradiation and superimposed UV light, after 333 h of stability test b) EIS measurement at OCP of a UV temporarily illuminated degraded photoanode, partially recovering the photocurrent via light-induced states. Measurements performed under 1 sun illumination, using 1 M KOH as electrolyte.

Similar stability test was performed with a $p^+$-n-Si photoanode with $TiO_2$ deposited at 300 ºC and NiFe decorated. Likewise, after 333 h at 1.3 V vs RHE photocurrent has been reduced significantly (Figure S14).

To validate the previously described degradation mechanism, superimposed UV illumination was used to modify the density of states within the $TiO_2$electronic structure, achieving a significant recovery of the photocurrent (Figure 7a). This can be explained by the photoconductivity effect on $TiO_2$,[100] where the UV photons create electron-hole pairs changing the occupation of localized states, causing a significant reduction of $R_2$ (Figure 7b, Table S1).[101] Switching off UV light gave a few-seconds decay followed by a several minutes persistent photoconductivity (PPC). These states created by oxygen desorption will eventually be

compensated again by $OH^-$ diffusing inside the material, as illustrated in Scheme S1. This UV-light effect should only be expected in the near-surface region of $TiO_2$ due to small UV photon penetration depth, precisely where higher $OH^-$ interaction would be.

## 4. CONCLUSIONS

$TiO_2$ protective layers grown by ALD have been deposited on silicon photoanodes to avoid corrosion, while allowing charge transfer to the electrolyte to perform the oxygen evolution reaction using a NiFe earth abundant catalyst. Layers consisting of approximately 100 nm have been grown at 100, 150 and 300 ºC, corresponding to completely amorphous, partially crystalline and fully crystalline $TiO_2$.

Completely amorphous layers presented high resistivity, meanwhile the ones synthetized at 300ºC, having a fully anatase crystalline $TiO_2$ structure, introduced insignificant resistance, showing direct correlation between crystallization degree and electrical conductivity. The conductivity through crystalline $TiO_2$ layers has been found not to be homogeneous, presenting preferential conduction paths attributed to grain boundaries and defects within the crystalline structure. A correlation between the c-AFM measurements and grain interstitials can be seen, supported by HRTEM cross sectional images presenting defective regions in crystalline $TiO_2$ grains.

A conduction mechanism has been proposed assuming electrons coming from water oxidation are injected into the $TiO_2$ conduction band in preferential regions through the electrocatalyst. Then, electrons are transported to the $Si/SiO_x/TiO_2$ interface where electrons recombine with holes given by the $p^+n$-Si junction. No evidences of intra band gap states in $TiO_2$ responsible of conductivity have been detected.

On the other hand, current decay under continuous polarization was found, where $OH^-$ ions are considered to diffuse into $TiO_2$ under anodic conditions and alter conduction paths conductivity. These changes were analysed under long-time (> 480 h) stability measurements at fixed voltage, which presented current decay over time. Deeper EIS analysis show two different time constant RC elements changing during endurance test, and allowed to track electrical variations in a series circuit structure. Associated $TiO_2$ resistance increases logarithmically over time, as expected for metal oxide surface passivation, corroborating a self-limited degradation. A 5 times increase on the EIS measured resistances associated to $TiO_2$ conductivity and OER catalysis is in accordance with the total current reduction observed after 480 h stability test in anodic polarization.

To corroborate this model, UV illumination was used to modify states occupancy, presenting persistent conductivity thanks to the partial recovery of the electronic states lost under working conditions. Further studies focused on higher resolution analysis than this work are needed to identify $OH^-$ diffusion into $TiO_2$ structure and states loss, specifically in preferential regions. UV illumination constitutes a promising method to partially recover degradation. This confirms that the degradation mechanisms of $TiO_2$ still needs to be taken into consideration to enhance its long term use endurance as a transparent conductive and protective layer for frontal illumination water splitting photoanodes.

## ASSOCIATED CONTENT

AFM, HRTEM, XPS, and EIS supplementary data, together with a photo of a finished device and a scheme of UV recovery, are supplied in an additional document

## AUTHOR INFORMATION

### **Corresponding Author**

*cros@irec.cat

*tandreu@irec.cat

**Author Contributions**

The manuscript was written through contributions of all authors. All authors have given approval to the final version of the manuscript.

**ACKNOWLEDGMENT**

This work was partially supported by Repsol, S.A. and Enagas S.A. Authors from IREC thank Generalitat de Catalunya for financial support through the CERCA Programme, M2E (2017SGR1246) and XaRMAE network. IREC also acknowledges additional support by the European Regional Development Funds (ERDF, FEDER) and by MINECO coordinated projects MAT2014-59961-C2 and ENE2016-80788-C5-5-R. C.R. thanks to MINECO for his FPI grant (BES-2015-071618). ICN2 acknowledge funding from Generalitat de Catalunya 2017 SGR 327 and the Spanish MINECO project ENE2017-85087-C3. ICN2 is supported by the Severo Ochoa program from Spanish MINECO (Grant No. SEV-2017-0706) and is funded by the CERCA Programme / Generalitat de Catalunya. JD has received funding from the European Union's Horizon 2020 research and innovation programme under the Marie Sklodowska-Curie grant agreement No 665919 (P-SPHERE) co-funded by Severo Ochoa Programme.

**REFERENCES**

(1) Lewis, N. S.; Nocera, D. G. Powering the Planet: Chemical Challenges in Solar Energy

Utilization. *Proc. Natl. Acad. Sci. U. S. A.* **2006**, *103* (43), 15729–15735.

(2) Wang, M. Fuel Choices for Fuel-Cell Vehicles: Well-to-Wheels Energy and Emission Impacts. *J. Power Sources* **2002**, *112* (1), 307–321.

(3) James, B. D.; Baum, G. N.; Perez, J.; Baum, K. N. Technoeconomic Analysis of Photoelectrochemical (PEC) Hydrogen Production. **2009**, 1–128.

(4) Barber, J.; Tran, P. D. From Natural to Artificial Photosynthesis. *J. R. Soc. Interface* **2013**, *10* (81), 20120984.

(5) Haeseldonckx, D.; D'haeseleer, W. The Use of the Natural-Gas Pipeline Infrastructure for Hydrogen Transport in a Changing Market Structure. *Int. J. Hydrogen Energy* **2007**, *32* (10–11), 1381–1386.

(6) Berry, G. D.; Pasternak, A. D.; Rambach, G. D.; Smith, J. R.; Schock, R. N. Hydrogen as a Future Transportation Fuel. *Energy* **1996**, *21* (4), 289–303.

(7) Fujishima, A.; Honda, K. Electrochemical Photolysis of Water at a Semiconductor Electrode. *Nature* **1972**, *238* (5358), 37–38.

(8) Bard, A. J.; Fox, M. A. Artificial Photosynthesis: Solar Splitting of Water to Hydrogen and Oxygen Water Splitting. *Acc. Chem. Res* **1995**, *28*, 141–145.

(9) Murphy, A. B.; Barnes, P. R. F.; Randeniya, L. K.; Plumb, I. C.; Grey, I. E.; Horne, M. D.; Glasscock, J. A. Efficiency of Solar Water Splitting Using Semiconductor Electrodes. *Int. J. Hydrogen Energy* **2006**, *31* (14), 1999–2017.

(10) Ros, C.; Fabrega, C.; Monllor-Satoca, D.; Hernández-Alonso, M. D.; Penelas-Pérez, G.; Morante, J. R.; Andreu, T. Hydrogenation and Structuration of $TiO_2$ Nanorods Photoanodes: Doping Level and the Effect of Illumination in Trap-States Filling. *J. Phys. Chem. C* **2018**, *122* (6), 3295–3304.

(11) Ni, M.; Leung, M. K. H.; Leung, D. Y. C.; Sumathy, K. A Review and Recent Developments in Photocatalytic Water-Splitting Using $TiO_2$ for Hydrogen Production. *Renew. Sustain.*

*Energy Rev.* **2007**, *11* (3), 401–425.

(12) Maeda, K.; Domen, K. Photocatalytic Water Splitting: Recent Progress and Future Challenges. *J. Phys. Chem. Lett.* **2010**, *1* (18), 2655–2661.

(13) Fàbrega, C.; Andreu, T.; Cabot, A.; Morante, J. R. Location and Catalytic Role of Iron Species in TiO2:Fe Photocatalysts: An EPR Study. *J. Photochem. Photobiol. A Chem.* **2010**, *211* (2–3), 170–175.

(14) Murcia-López, S.; Hidalgo, M. C.; Navío, J. A. Synthesis, Characterization and Photocatalytic Activity of Bi-Doped $TiO_2$ Photocatalysts under Simulated Solar Irradiation. *Appl. Catal. A Gen.* **2011**, *404* (1–2), 59–67.

(15) Sivula, K.; Formal, F. Le; Grätzel, M. $WO_3$ −$Fe_2O_3$ Photoanodes for Water Splitting: A Host Scaffold, Guest Absorber Approach. *Chem. Mater.* **2009**, *21* (13), 2862–2867.

(16) Fàbrega, C.; Murcia-López, S.; Monllor-Satoca, D.; Prades, J. D.; Hernández-Alonso, M. D.; Penelas, G.; Morante, J. R.; Andreu, T. Efficient $WO_3$ Photoanodes Fabricated by Pulsed Laser Deposition for Photoelectrochemical Water Splitting with High Faradaic Efficiency. *Appl. Catal. B Environ.* **2016**, *189*, 133–140.

(17) Murcia-López, S.; Fabrega, C.; Monllor-Satoca, D.; Hernández-Alonso, M. D.; Penelas-Pérez, G.; Morata, A.; Morante, J. R.; Andreu, T.; Fàbrega, C.; Monllor-Satoca, D.; et al. Tailoring Multilayered $BiVO_4$ Photoanodes by Pulsed Laser Deposition for Water Splitting. *ACS Appl. Mater. Interfaces* **2016**, *8* (6), 4076–4085.

(18) Tang, P.; Xie, H.; Ros, C.; Han, L.; Biset-Peiró, M.; He, Y.; Kramer, W.; Rodríguez, A. P.; Saucedo, E.; Galán-Mascarós, J. R.; et al. Enhanced Photoelectrochemical Water Splitting of Hematite Multilayer Nanowire Photoanodes by Tuning the Surface State via Bottom-up Interfacial Engineering. *Energy Environ. Sci.* **2017**, *10* (10), 2124–2136.

(19) Chu, S.; Li, W.; Yan, Y.; Hamann, T.; Shih, I.; Wang, D.; Mi, Z. Roadmap on Solar Water Splitting : Current Status and Future Prospects. **2017**.

(20) Bae, D.; Seger, B.; Vesborg, P. C. K.; Hansen, O.; Chorkendorff, I. Strategies for Stable

Water Splitting via Protected Photoelectrodes. *Chem. Soc. Rev.* **2017**, *46* (7), 1933–1954.

(21) Wang, T.; Gong, J. Single-Crystal Semiconductors with Narrow Band Gaps for Solar Water Splitting. *Angew. Chemie - Int. Ed.* **2015**, *54* (37), 10718–10732.

(22) Ros, C.; Andreu, T.; Hernández-Alonso, M. D.; Penelas-Pérez, G.; Arbiol, J.; Morante, J. R. Charge Transfer Characterization of ALD-Grown $TiO_2$ Protective Layers in Silicon Photocathodes. *ACS Appl. Mater. Interfaces* **2017**, *9*, 17932–17941.

(23) Seger, B.; Laursen, A. B.; Vesborg, P. C. K.; Pedersen, T.; Hansen, O.; Dahl, S.; Chorkendorff, I. Hydrogen Production Using a Molybdenum Sulfide Catalyst on a Titanium-Protected n(+)p-Silicon Photocathode. *Angew. Chem. Int. Ed. Engl.* **2012**, *51* (36), 9128–9131.

(24) McKone, J. R.; Warren, E. L.; Bierman, M. J.; Boettcher, S. W.; Brunschwig, B. S.; Lewis, N. S.; Gray, H. B. Evaluation of Pt, Ni, and Ni–Mo Electrocatalysts for Hydrogen Evolution on Crystalline Si Electrodes. *Energy Environ. Sci.* **2011**, *4* (9), 3573–3583.

(25) Turan, B.; Becker, J.-P.; Urbain, F.; Finger, F.; Rau, U.; Haas, S. Upscaling of Integrated Photoelectrochemical Water-Splitting Devices to Large Areas. *Nat. Commun.* **2016**, *7*, 12681.

(26) Ros, C.; Andreu, T.; Giraldo, S.; Sánchez, Y.; Morante, J. R. Conformal Chalcopyrite Based Photocathode for Solar Refinery Applications. *Sol. Energy Mater. Sol. Cells* **2016**, *158*, 184–188.

(27) Ros, C.; Andreu, T.; Giraldo, S.; Izquierdo-Roca, V.; Saucedo, E.; Morante, J. R. Turning Earth Abundant Kesterite-Based Solar Cells into Efficient Protected Water Splitting Photocathodes. *ACS Appl. Mater. Interfaces* **2018**, *10*, 13425−13433.

(28) Hu, S.; Shaner, M. R.; Beardslee, J. a; Lichterman, M.; Brunschwig, B. S.; Lewis, N. S. Amorphous $TiO_2$ Coatings Stabilize Si, GaAs, and GaP Photoanodes for Efficient Water Oxidation. *Science* **2014**, *344* (6187), 1005–1009.

(29) Khaselev, O.; Turner, J. A.; Khaselev, O.; Turner, J. A. A Monolithic Photovoltaic-

Photoelectrochemical Device for Hydrogen Production via Water Splitting R EPORTS A Monolithic Photovoltaic-Photoelectrochemical Device for Hydrogen Production via Water Splitting. *Science (80-. ).* **1998**, *280*, 425–429.

(30) Tang, S. J.; Moniz, S. J. A.; Shevlin, S. A.; Martin, D. J.; Guo, Z.-X.; Tang, J. Visible-Light Driven Heterojunction Photocatalysts for Water Splitting – a Critical Review. *Energy Environ. Sci.* **2015**, *8*, 731–759.

(31) Lee, M. H.; Takei, K.; Zhang, J.; Kapadia, R.; Zheng, M.; Chen, Y.-Z.; Nah, J.; Matthews, T. S.; Chueh, Y.-L.; Ager, J. W.; et al. P-Type InP Nanopillar Photocathodes for Efficient Solar-Driven Hydrogen Production. *Angew. Chemie Int. Ed.* **2012**, *51* (43), 10760–10764.

(32) Sun, K.; Kuang, Y.; Verlage, E.; Brunschwig, B. S.; Tu, C. W.; Lewis, N. S. Sputtered $NiO_x$ Films for Stabilization of P+n-InP Photoanodes for Solar-Driven Water Oxidation. *Adv. Energy Mater.* **2015**.

(33) Guerrero, A.; Bisquert, J. Perovskite Semiconductors for Photoelectrochemical Water Splitting Applications. *Curr. Opin. Electrochem.* **2017**, *2* (1), 144–147.

(34) Liu, R.; Zheng, Z.; Spurgeon, J.; Yang, X. Enhanced Photoelectrochemical Water-Splitting Performance of Semiconductors by Surface Passivation Layers. *Energy Environ. Sci.* **2014**, *7* (8), 2504–2517.

(35) Hu, S.; Lewis, N. S.; Ager, J. W.; Yang, J.; McKone, J. R.; Strandwitz, N. C. Thin-Film Materials for the Protection of Semiconducting Photoelectrodes in Solar-Fuel Generators. *J. Phys. Chem. C* **2015**, *119* (43), 24201–24228.

(36) Lichterman, M. F.; Sun, K.; Hu, S.; Zhou, X.; McDowell, M. T.; Shaner, M. R.; Richter, M. H.; Crumlin, E. J.; Carim, A. I.; Saadi, F. H.; et al. Protection of Inorganic Semiconductors for Sustained, Efficient Photoelectrochemical Water Oxidation. *Catal. Today* **2016**, *262*, 11–23.

(37) Lewis, N. S. Developing a Scalable Artificial Photosynthesis Technology through Nanomaterials by Design. *Nat. Nanotechnol.* **2016**, *11* (12), 1010–1019.

(38) Digdaya, I. A.; Adhyaksa, G. W. P.; Trzesniewski, B. J.; Garnett, E. C.; Smith, W. A. Interfacial Engineering of Metal-Insulator-Semiconductor Junctions for Efficient and Stable Photoelectrochemical Water Oxidation. *Nat. Commun.* **2017**, *8* (May), 15968.

(39) Wang, T.; Luo, Z.; Li, C.; Gong, J. Controllable Fabrication of Nanostructured Materials for Photoelectrochemical Water Splitting via Atomic Layer Deposition. *Chem. Soc. Rev.* **2014**, *43* (22), 7469–7484.

(40) Wen, L.; Zhou, M.; Wang, C.; Mi, Y.; Lei, Y. Nanoengineering Energy Conversion and Storage Devices via Atomic Layer Deposition. *Adv. Energy Mater.* **2016**, *6* (23), 1600468.

(41) Miikkulainen, V.; Leskelä, M.; Ritala, M.; Puurunen, R. L.; Leskelä, M.; Ritala, M.; Puurunen, R. L. Crystallinity of Inorganic Films Grown by Atomic Layer Deposition: Overview and General Trends. *J. Appl. Phys.* **2013**, *113* (2), 021301.

(42) Seger, B.; Tilley, D. S.; Pedersen, T.; Vesborg, P. C. K.; Hansen, O.; Grätzel, M.; Chorkendorff, I. Silicon Protected with Atomic Layer Deposited $TiO_2$: Durability Studies of Photocathodic $H_2$ Evolution. *RSC Adv.* **2013**, *3* (48), 25902–25907.

(43) Tang-Kong, R.; Winter, R.; Brock, R.; Tracy, J.; Eizenberg, M.; Dauskardt, R. H.; McIntyre, P. C. The Role of Catalyst Adhesion in ALD-$TiO_2$ Protection of Water Splitting Silicon Anodes. *ACS Appl. Mater. Interfaces* **2018**, *10* (43), 37103–37109.

(44) Karbalaei Akbari, M.; Hai, Z.; Wei, Z.; Detavernier, C.; Solano, E.; Verpoort, F.; Zhuiykov, S. ALD-Developed Plasmonic Two-Dimensional Au-$WO_3$-$TiO_2$ Heterojunction Architectonics for Design of Photovoltaic Devices. *ACS Appl. Mater. Interfaces* **2018**, *10* (12), 10304–10314.

(45) Seger, B.; Pedersen, T.; Laursen, A. B.; Vesborg, P. C. K.; Hansen, O.; Chorkendorff, I. Using $TiO_2$ as a Conductive Protective Layer for Photocathodic $H_2$ Evolution. *J. Am. Chem. Soc.* **2013**, *135* (3), 1057–1064.

(46) Seger, B.; Tilley, S. D.; Pedersen, T.; Vesborg, P. C. K.; Hansen, O.; Graetzel, M.; Chorkendorff, I. Silicon Protected with Atomic Layer Deposited $TiO_2$: Conducting versus Tunnelling through $TiO_2$. *J. Mater. Chem. a* **2013**, *1* (47), 15089–15094.

(47) Bae, D.; Shayestehaminzadeh, S.; Thorsteinsson, E. B.; Pedersen, T.; Hansen, O.; Seger, B.; Vesborg, P. C. K.; Ólafsson, S.; Chorkendorff, I. Protection of Si Photocathode Using $TiO_2$ Deposited by High Power Impulse Magnetron Sputtering for $H_2$ Evolution in Alkaline Media. *Sol. Energy Mater. Sol. Cells* **2016**, *144* (JANUARY), 758–765.

(48) Gu, J.; Aguiar, J. A.; Ferrere, S.; Steirer, K. X.; Yan, Y.; Xiao, C.; Young, J. L.; Al-jassim, M.; Neale, N. R.; Turner, J. A. A Graded Catalytic–protective Layer for an e Cient and Stable Water-Splitting Photocathode. **2017**, No. January, 1–8.

(49) Engel, J.; Bishop, S. R.; Vayssieres, L.; Tuller, H. L. In Situ Electrical Characterization of Anatase $TiO_2$ Quantum Dots. *Adv. Funct. Mater.* **2014**, *24* (31), 4952–4958.

(50) Chen, Y. W.; Prange, J. D.; Dühnen, S.; Park, Y.; Gunji, M.; Chidsey, C. E. D.; McIntyre, P. C. Atomic Layer-Deposited Tunnel Oxide Stabilizes Silicon Photoanodes for Water Oxidation. *Nat. Mater.* **2011**, *10* (7), 539–544.

(51) Scheuermann, A. G.; Prange, J. D.; Gunji, M.; Chidsey, C. E. D.; McIntyre, P. C. Effects of Catalyst Material and Atomic Layer Deposited $TiO_2$ Oxide Thickness on the Water Oxidation Performance of Metal–insulator–silicon Anodes. *Energy Environ. Sci.* **2013**, *6* (8), 2487.

(52) Satterthwaite, P. F.; Scheuermann, A. G.; Hurley, P. K.; Chidsey, C. E. D.; McIntyre, P. C. Engineering Interfacial Silicon Dioxide for Improved Metal-Insulator-Semiconductor Silicon Photoanode Water Splitting Performance. *ACS Appl. Mater. Interfaces* **2016**, *8* (20), 13140–13149.

(53) McDowell, M. T.; Lichterman, M. F.; Carim, A. I.; Liu, R.; Hu, S.; Brunschwig, B. S.; Lewis, N. S. The Influence of Structure and Processing on the Behavior of $TiO_2$ Protective Layers for Stabilization of n-Si/$TiO_2$ /Ni Photoanodes for Water Oxidation. *ACS Appl. Mater. Interfaces* **2015**, *7* (28), 15189–15199.

(54) Hu, S.; Richter, M. H.; Lichterman, M. F.; Beardslee, J.; Mayer, T.; Brunschwig, B. S.; Lewis, N. S. Electrical, Photoelectrochemical, and Photoelectron Spectroscopic Investigation of the Interfacial Transport and Energetics of Amorphous TiO2/Si

Heterojunctions. *J. Phys. Chem. C* **2016**, *120* (6), 3117–3129.

(55) Xia, Z.; Zhou, X.; Li, J.; Qu, Y. Protection Strategy for Improved Catalytic Stability of Silicon Photoanodes for Water Oxidation. *Sci. Bull.* **2015**, *60* (16), 1395–1402.

(56) Mei, B.; Pedersen, T.; Malacrida, P.; Bae, D.; Frydendal, R.; Hansen, O.; Vesborg, P. C. K.; Seger, B.; Chorkendorff, I. Crystalline $TiO_2$ : A Generic and Effective Electron-Conducting Protection Layer for Photoanodes and -Cathodes. *J. Phys. Chem. C* **2015**, *119* (27), 15019–15027.

(57) Scheuermann, A. G.; Lawrence, J. P.; Kemp, K. W.; Ito, T.; Walsh, A.; Chidsey, C. E. D.; Hurley, P. K.; McIntyre, P. C. Design Principles for Maximizing Photovoltage in Metal-Oxide-Protected Water-Splitting Photoanodes. *Nat. Mater.* **2016**, *15* (1), 99–105.

(58) Moehl, T.; Suh, J.; Sévery, L.; Wick-Joliat, R.; Tilley, S. D. Investigation of (Leaky) ALD TiO2 Protection Layers for Water Splitting Photoelectrodes. *ACS Appl. Mater. Interfaces* **2017**, acsami.7b12564.

(59) Campet, G.; Manaud, J. P.; Puprichitkun, C.; Sun, Z. W.; Salvador, P. Protection of Photoanodes against Photo-Corrosion by Surface Deposition of Oxide Films: Criteria for Choosing the Protective Coating. *Act. Passiv. Electron. Components* **1989**, *13* (3), 175–189.

(60) Aarik, J.; Aidla, A.; Uustare, T.; Sammelselg, V. Morphology and Structure of $TiO_2$ Thin Films Grown by Atomic Layer Deposition. *J. Cryst. Growth* **1995**, *148* (3), 268–275.

(61) Reiners, M.; Xu, K.; Aslam, N.; Devi, A.; Waser, R.; Hoffmann-Eifert, S. Growth and Crystallization of $TiO_2$ Thin Films by Atomic Layer Deposition Using a Novel Amido Guanidinate Titanium Source and Tetrakis-Dimethylamido-Titanium. *Chem. Mater.* **2013**, *25* (15), 2934–2943.

(62) Scheuermann, A. G.; Lawrence, J. P.; Meng, A. C.; Tang, K.; Hendricks, O. L.; Chidsey, C. E. D.; McIntyre, P. C. Titanium Oxide Crystallization and Interface Defect Passivation for High Performance Insulator-Protected Schottky Junction MIS Photoanodes. *ACS Appl. Mater. Interfaces* **2016**, *8* (23), 14596–14603.

(63) Heiss, M.; Conesa-Boj, S.; Ren, J.; Tseng, H. H.; Gali, A.; Rudolph, A.; Uccelli, E.; Peiró, F.; Morante, J. R.; Schuh, D.; et al. Direct Correlation of Crystal Structure and Optical Properties in Wurtzite/Zinc-Blende GaAs Nanowire Heterostructures. *Phys. Rev. B - Condens. Matter Mater. Phys.* **2011**, *83* (4), 1–11.

(64) Ohsaka, T.; Izumi, F.; Fujiki, Y. Raman Spectrum of Anatase, TiO2. *J. Raman Spectrosc.* **1978**, *7* (6), 321–324.

(65) Guerra-Nuñez, C.; Zhang, Y.; Li, M.; Chawla, V.; Erni, R.; Michler, J.; Park, H. G.; Utke, I. Morphology and Crystallinity Control of Ultrathin TiO2 Layers Deposited on Carbon Nanotubes by Temperature-Step Atomic Layer Deposition. *Nanoscale* **2015**, *7* (24), 10622–10633.

(66) Gupta, S. K.; Desai, R.; Jha, P. K.; Sahoo, S.; Kirin, D. Titanium Dioxide Synthesized Using Titanium Chloride: Size Effect Study Using Raman Spectroscopy and Photoluminescence. *J. Raman Spectrosc.* **2010**, *41* (3), 350–355.

(67) Saga, T. Advances in Crystalline Silicon Solar Cell Technology for Industrial Mass Production. *NPG Asia Mater.* **2010**, *2* (3), 96–102.

(68) Chen, L.; Toma, F. M.; Cooper, J. K.; Lyon, A.; Lin, Y.; Sharp, I. D.; Ager, J. W. Mo-Doped BiVO $_4$ Photoanodes Synthesized by Reactive Sputtering. *ChemSusChem* **2015**, *8* (6), 1066–1071.

(69) Smith, W. A.; Sharp, I. D.; Strandwitz, N. C.; Bisquert, J. Interfacial Band-Edge Energetics for Solar Fuels Production. *Energy Environ. Sci.* **2015**, *8* (10), 2851–2862.

(70) Mills, T. J.; Lin, F.; Boettcher, S. W. Theory and Simulations of Electrocatalyst-Coated Semiconductor Electrodes for Solar Water Splitting. *Phys. Rev. Lett.* **2014**, *112* (14), 1–5.

(71) Lichterman, M. F.; Hu, S.; Richter, M. H.; Crumlin, E.; Axnanda, S.; Favaro, M.; Drisdell, W. S.; Hussain, Z.; Mayer, T.; Brunschwig, B. S.; et al. Direct Observation of the Energetics at a Semiconductor/Liquid Junction by Operando X-Ray Photoelectron Spectroscopy. *Energy Environ. Sci.* **2015**, *8*, 2409–2416.

(72) Louie, M. W.; Bell, A. T. An Investigation of Thin-Film Ni-Fe Oxide Catalysts for the Electrochemical Evolution of Oxygen. *J. Am. Chem. Soc.* **2013**, *135* (33), 12329–12337.

(73) Corrigan, D. A. The Catalysis of the Oxygen Evolution Reaction by Iron Impurities in Thin Film Nickel Oxide Electrodes. *J. Electrochem. Soc.* **1987**, *134* (2), 377.

(74) Biset-Peiró, M.; Murcia-López, S.; Fàbrega, C.; Morante, J. R.; Andreu, T. Multilayer Ni/Fe Thin Films as Oxygen Evolution Catalysts for Solar Fuel Production. *J. Phys. D. Appl. Phys.* **2017**, *50* (10), 104003.

(75) Gong, M.; Dai, H. A Mini Review of NiFe-Based Materials as Highly Active Oxygen Evolution Reaction Electrocatalysts. *Nano Res.* **2014**, *8* (1), 23–39.

(76) Kenney, M. J.; Gong, M.; Li, Y.; Wu, J. Z.; Feng, J.; Lanza, M.; Dai, H. High-Performance Silicon Photoanodes Passivated with Ultrathin Nickel Films for Water Oxidation. *Science (80-. ).* **2013**, *342* (6160), 836–840.

(77) Kiseok Oh, a Cristelle Meriadec, b Benedikt Lassalle-Kaiser, c Vincent Dorcet, a Bruno Fabre, A.; Soraya Ababou-Girard, b Loic Joanny, d F. G. and G. L.; Oh, K.; Meriadec, C.; Lassalle-Kaiser, B.; Dorcet, V.; Fabre, B.; Ababou-Girard, S.; Joanny, L.; Gouttefangeas, F.; et al. Elucidating the Performance and Unexpected Stability of Partially Coated Water-Splitting Silicon Photoanodes. *Energy Environ. Sci.* **2018**, 0–11.

(78) Dette, C.; Hurst, M. R.; Deng, J.; Nellist, M. R.; Boettcher, S. W. Structural Evolution of Metal (Oxy)Hydroxide Nanosheets during the Oxygen Evolution Reaction. **2018**.

(79) Trotochaud, L.; Young, S. L.; Ranney, J. K.; Boettcher, S. W. Nickel-Iron Oxyhydroxide Oxygen-Evolution Electrocatalysts: The Role of Intentional and Incidental Iron Incorporation. *J. Am. Chem. Soc.* **2014**, *136* (18), 6744–6753.

(80) Nardi, K. L.; Yang, N.; Dickens, C. F.; Strickler, A. L.; Bent, S. F. Creating Highly Active Atomic Layer Deposited NiO Electrocatalysts for the Oxygen Evolution Reaction. *Adv. Energy Mater.* **2015**, *5* (17), 1–10.

(81) Zhu, K.; Luo, W.; Zhu, G.; Wang, J.; Zhu, Y.; Zou, Z.; Huang, W. Interface-Engineered

Ni(OH)2 /β-like FeOOH Electrocatalysts for Highly Efficient and Stable Oxygen Evolution Reaction. *Chem. - An Asian J.* **2017**, *12* (20), 2720–2726.

(82) Yu, Y.; Sun, C.; Yin, X.; Li, J.; Cao, S.; Zhang, C.; Voyles, P. M.; Wang, X. Metastable Intermediates in Amorphous Titanium Oxide: A Hidden Role Leading to Ultra-Stable Photoanode Protection. *Nano Lett.* **2018**, *18* (8), 5335–5342.

(83) Murakami, K.; Rommel, M.; Hudec, B.; Rosová, A.; Hušeková, K.; Dobročka, E.; Rammula, R.; Kasikov, A.; Han, J. H.; Lee, W.; et al. Nanoscale Characterization of $TiO_2$ Films Grown by Atomic Layer Deposition on $RuO_2$ Electrodes. *ACS Appl. Mater. Interfaces* **2014**, *6* (4), 2486–2492.

(84) Tang, K.; Meng, A. C.; Hui, F.; Shi, Y.; Petach, T.; Hitzman, C.; Koh, A. L.; Goldhaber-Gordon, D.; Lanza, M.; McIntyre, P. C. Distinguishing Oxygen Vacancy Electromigration and Conductive Filament Formation in $TiO_2$ Resistance Switching Using Liquid Electrolyte Contacts. *Nano Lett.* **2017**, *17* (7), 4390–4399.

(85) Kim, S. K.; Kim, K. M.; Jeong, D. S.; Jeon, W.; Yoon, K. J.; Hwang, C. S. Titanium Dioxide Thin Films for Next-Generation Memory Devices. *J. Mater. Res.* **2013**, *28* (3), 313–325.

(86) Du, Y.; Kumar, A.; Pan, H.; Zeng, K.; Wang, S.; Yang, P.; Wee, A. T. S. The Resistive Switching in TiO2films Studied by Conductive Atomic Force Microscopy and Kelvin Probe Force Microscopy. *AIP Adv.* **2013**, *3* (8).

(87) Kwon, D. H.; Kim, K. M.; Jang, J. H.; Jeon, J. M.; Lee, M. H.; Kim, G. H.; Li, X. S.; Park, G. S.; Lee, B.; Han, S.; et al. Atomic Structure of Conducting Nanofilaments in $TiO_2$ Resistive Switching Memory. *Nat. Nanotechnol.* **2010**, *5* (2), 148–153.

(88) Han, T.; Shi, Y.; Song, X.; Mio, A.; Valenti, L.; Hui, F.; Privitera, S.; Lombardo, S.; Lanza, M. Ageing Mechanisms of Highly Active and Stable Nickel-Coated Silicon Photoanodes for Water Splitting. *J. Mater. Chem. A* **2016**, *4* (21), 8053–8060.

(89) Biesinger, M. C.; Lau, L. W. M.; Gerson, A. R.; Smart, R. S. C. The Role of the Auger Parameter in XPS Studies of Nickel Metal, Halides and Oxides. *Phys. Chem. Chem. Phys.* **2012**, *14* (7), 2434–2442.

(90) Zhou, H.; Yu, F.; Zhu, Q.; Sun, J.; Qin, F.; Yu, L.; Bao, J.; Yu, Y. Water Splitting by Electrolysis at High Current Density under 1.6 Volt. *Energy Environ. Sci.* **2018**, No. 60 mL, 3–5.

(91) Biesinger, M. C.; Payne, B. P.; Grosvenor, A. P.; Lau, L. W. M.; Gerson, A. R.; Smart, R. S. C. Resolving Surface Chemical States in XPS Analysis of First Row Transition Metals, Oxides and Hydroxides: Cr, Mn, Fe, Co and Ni. *Appl. Surf. Sci.* **2011**, *257* (7), 2717–2730.

(92) Mei, B.; Permyakova, A. a; Frydendal, R.; Bae, D.; Pedersen, T.; Malacrida, P.; Hansen, O.; Stephens, I. E. L.; Vesborg, P. C. K.; Seger, B.; et al. Iron-Treated NiO as a Highly Transparent p - Type Protection Layer for E Ffi Cient Si-Based Photoanodes. *J. Phys. Chem. Lett.* **2014**, *5* (20), 3456–3461.

(93) Seger, B.; Bae, D.; Seger, B.; Vesborg, P. C. K.; Hansen, O.; Chorkendorff, I. Strategies for Stable Water Splitting via Protected. *Chem. Soc. Rev.* **2017**, *46* (7), 1933–1954.

(94) Samin, A. J.; Taylor, C. D. An Analysis of Limiting Cases for the Metal Oxide Film Growth Kinetics Using an Oxygen Defects Model Accounting for Transport and Interfacial Reactions. **2018**, *43* (4), 317–326.

(95) Hannula, M.; Ali-Löytty, H.; Lahtonen, K.; Sarlin, E.; Saari, J.; Valden, M. Improved Stability of Atomic Layer Deposited Amorphous $TiO_2$ Photoelectrode Coatings by Thermally Induced Oxygen Defects. *Chem. Mater.* **2018**, acs.chemmater.7b02938.

(96) Tang, K.; Meng, A. C.; Hui, F.; Shi, Y.; Petach, T.; Hitzman, C.; Koh, A. L.; Goldhaber-Gordon, D.; Lanza, M.; McIntyre, P. C. Distinguishing Oxygen Vacancy Electromigration and Conductive Filament Formation in TiO2Resistance Switching Using Liquid Electrolyte Contacts. *Nano Lett.* **2017**, *17* (7), 4390–4399.

(97) Kim, K. M.; Jeong, D. S.; Hwang, C. S. Nanofilamentary Resistive Switching in Binary Oxide System; A Review on the Present Status and Outlook. *Nanotechnology* **2011**, *22* (25).

(98) Agrell, H. G.; Boschloo, G.; Hagfeldt, A. Conductivity Studies of Nanostructured $TiO_2$ Films Permeated with Electrolyte. *J. Phys. Chem. B* **2004**, *108* (33), 12388–12396.

(99) Han, L.; Tang, P.; Reyes-Carmona, Á.; Rodríguez-García, B.; Torréns, M.; Morante, J. R.; Arbiol, J.; Galan-Mascaros, J. R. Enhanced Activity and Acid PH Stability of Prussian Blue-Type Oxygen Evolution Electrocatalysts Processed by Chemical Etching. *J. Am. Chem. Soc.* **2016**, *138* (49), 16037–16045.

(100) Fàbrega, C.; Hernández-Ramírez, F.; Daniel Prades, J.; Jiménez-Díaz, R.; Andreu, T.; Ramon Morante, J. On the Photoconduction Properties of Low Resistivity TiO2 Nanotubes. *Nanotechnology* **2010**, *21* (44).

(101) Nakajima, A.; Watanabe, T.; Wang, R.; Hashimoto, K.; Minabe, M.; Koizumi, S.; Fujishima, A. Photocatalytic Activity and Photoinduced Hydrophilicity of Titanium Dioxide Coated Glass. *Thin Solid Films* **2002**, *351* (1–2), 260–263.

TOC

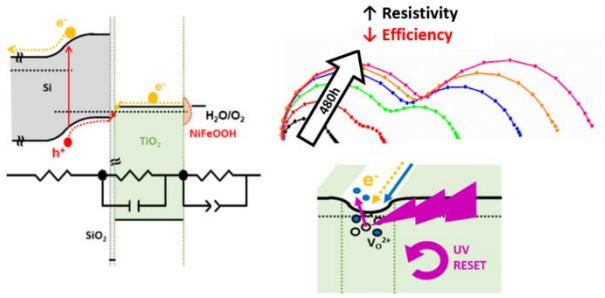
Si
$H_2O/O_2$
NiFeOOH
$TiO_2$
h+
$SiO_2$
↑ Resistivity
↓ Efficiency
480h
e-
$V_O^{2+}$
UV
RESET